Available online at www.sciencedirect.com

ScienceDirect

Underground Space 3 (2018) 218–228

www.elsevier.com/locate/undsp

Modeling hydraulic cracks and inclusion interaction using XFEM

Bo He [a], Xiaoying Zhuang [a,b,*]

[a] Institute of Continuum Mechanics, Leibniz Universität Hannover, 30167 Hannover, Germany
[b] College of Civil Engineering, Tongji University, Shanghai 200092, China

Received 26 February 2018; received in revised form 13 April 2018; accepted 18 April 2018
Available online 14 June 2018

Abstract

In this study, we employ a coupled hydromechanical model to study the hydraulic fracture propagation path in porous media under the influence of existing pressurized voids. The hydraulic fracturing field study reveals that the existing natural voids and cracks alter the local properties of the porous media and influence the fracture propagation pattern. We incorporate these phenomena into the presented hydromechanical model, which is constructed from the mass and momentum balance equations for saturated porous media. The extended finite element method (XFEM) is applied for modeling the fluid flow through discrete cracks. The nonlinear hydromechanical equations are solved by the Newton–Raphson scheme with an implicit time integration procedure. Finally, numerical examples are presented and compared with experimental results. It is found that the fracture propagation path is significantly influenced by the existing pressurized voids and essential properties of the porous media; that is, the crack trends to propagate towards the pressurized voids.

Keywords: Porous media; XFEM; Hydraulic fractures; Crack propagation

1 Introduction

Hydraulic fracturing is used extensively in the extraction of shell gas in the oil industry. In order to gain an improved understanding of hydraulic fracturing, it is of utmost importance to consider the fluid flow through the propagating fracture network (Bazant, 1984). At present, several numerical approaches are available that are capable of modeling hydraulic fracturing. These methods generally employ enrichment, remeshing or a meshless technique. For methods equipped with the enrichment technique, the extended finite element method (XFEM) (Belytschko & Black, 1999; Dolbow & Belytschko, 1999a,b) is one of the common approaches for modeling fractures. XFEM was developed in 1999 in order to model crack growth without remeshing. It is capable of modeling fluid-structure interaction (Gerstenberger & Wall, 2008; Wang & Belytschko, 2009) and fluid flow through cracks (Rabczuk, Gracie, Song, & Belytschko, 2010; Rabczuk, Zi, Bordas, & Nguyen-Xuan, 2010; Rethore, Borst, & Abellan, 2007). Other than XFEM, the phantom node method (Hansbo & Hansbo, 2004; Song, Areias, & Belytschko, 2006) introduces additional nodes to form overlapping elements for describing discontinuities (Rabczuk & Zi, 2007; Vu-Bac et al., 2013). However, the original phantom node method encounters difficulties when cracks do not penetrate the entire element. A special crack tip element has been proposed to address this issue and thereby allow for complex crack patterns (Chau-Dinh, Zi, Lee, Rabczuk, & Song, 2012; Rabczuk, Zi, Bordas, & Nguyen-Xuan, 2008; Rabczuk, Zi, & Gerstenberger, & Wall, 2008). Methods employing remeshing techniques (Areias, Dias-da-Costa, Sargado, & Rabczuk, 2013; Areias & Rabczuk, 2013; Areias, Rabczuk, & Camanho, 2013; Areias, Rabczuk, & Camanho, 2014; Areias, Rabczuk, & DiasdaCosta, 2013) are strong competitors

* Corresponding author at: Institute of Continuum Mechanics, Leibniz Universität Hannover, 30167 Hannover, Germany.
E-mail address: zhuang@ikm.uni-hannover.de (X. Zhuang).

https://doi.org/10.1016/j.undsp.2018.04.005

to the enriched method. These methods benefit from the rapid improvements in remeshing techniques over the past several decades, and methods with remeshing techniques avoid modification of the stiffness matrix owing to enrichments, as in the XFEM or phantom node method. Furthermore, remeshing has been used in cohesive element approaches (Ortiz & Pandolfi, 1999; Remmers, Borst, & Needleman, 2003) for dynamic fractures. The meshless method (Belytschko, Guo, Kam Liu, & Ping Xiao, 2000; Belytschko, Krongauz, Organ, Fleming, & Krysl, 1996; Dolbow & Belytschko, 1999a,b; Nguyen, Rabczuk, Bordas, & Duflot, 2008) is ideal for problems requiring a higher order continuity than C^1 and could avoid element distortion under large deformation, which is a common case in the standard FEM approach. Meshless approaches capture discrete cracks using techniques such as the visibility criterion (Belytschko & Tabbara, 1996), diffraction criterion (Organ, Fleming, Terry, & Belytschko, 1996), and transparency criterion (Organ et al., 1996). Newer approaches also exploit the concept of enrichment (Amiri, Anitescu, Arroyo, Bordas, & Rabczuk, 2014; Rabczuk & Areias, 2006; Rabczuk, Areias, & Belytschko, 2007; Rabczuk & Zi, 2007; Zi, Rabczuk, & Wall, 2007). Furthermore, meshless methods have been extended to highly complex 3D fractures (Bordas, Rabczuk, & Zi, 2008; Rabczuk, Bordas, & Zi, 2007a; Rabczuk, Zi, Bordas, et al., 2008; Rabczuk, Zi, & Gerstenberger, et al., 2008), including fractures owing to fluid-structure interaction (Rabczuk, Robert, et al., 2010). However, the computational costs for meshless methods are considerably higher than those of enriched or remeshing methods.

In addition to the above-mentioned methods, recently developed approaches such as phase field techniques (Areias, Msekh, & Rabczuk, 2016; Miehe, Welschinger, & Hofacker, 2010) and the cracking particles method (Rabczuk & Belytschko, 2004; Rabczuk, Bordas, & Zi, 2007b; Rabczuk, Zi, Bordas, et al., 2010b) are alternatives for modeling fractures. However, the phase field approaches smear the crack with a predefined width and thus cannot model the fluid flow in the cavity accurately. Meanwhile, the cracking particles method uses cracked nodes to describe the cracking and is therefore also not suitable for modeling the fluid flow inside the cavity. An interesting fracture method is peridynamics (PD) (Ren, Zhuang, Cai, & Rabczuk, 2016; Ren, Zhuang, & Rabczuk, 2016; Ren, Zhuang, & Rabczuk, 2017; Silling, Epton, Weckner, Xu, & Askari, 2007), which is a nonlocal theory that elegantly unifies continuous and discontinuous deformations; hence, fracturing is part of the solution and not the problem. However, modeling the fluid flow through discrete cracks is somewhat challenging in PD. In the shell gas extraction process, a field study (Gale, Reed, & Holder, 2007) demonstrated that the existing natural voids and fractures alter the local properties of porous media and make the fracturing process difficult to predict. Hence, it is crucial to consider the existing voids or fractures when characterizing the hydraulic fracture process.

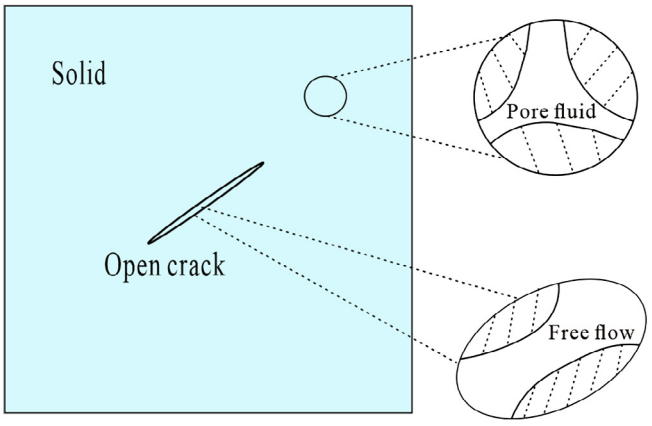

Fig. 1. Schematic illustration of fluid flow in fractured, deforming porous medium.

In this study, we present an extended finite element formulation for fluid flow in porous media (see Fig. 1). On the foundation of the model by (Rethore et al., 2007), we extended the model to include crack propagation. We validated the extended model by reproducing the experimental setup of (Bruno & Nakagawa, 1991) for the presented model. The comparison between the numerical and experimental results demonstrate that the extended model can accurately predict the crack propagation development in porous media under the influence of the pressurized zone. Furthermore, we found that the existing fluid pressure and essential properties of porous media are critical for determining the crack propagation path.

The remaining of this paper is organized as follows. We present the governing equations in their strong and weak form in Section 2. The XFEM formulation and discrete system of equations are presented in Sections 3 and 4. Subsequently, we present the computational results in Section 5, before concluding the manuscript in Section 6.

2 Governing equations for bulk

2.1 Strong form

2.1.1 Momentum balance

We assume a small displacement theory, no mass transfer between constituents, and isothermal conditions (Abellan & Borst, 2006). Hence, the momentum balance equation for a two-phase material is expressed as:

$$\nabla \cdot \boldsymbol{\sigma}_\pi + \hat{\boldsymbol{p}}_\pi + \rho_\pi \boldsymbol{g} = \frac{\partial(\rho_\pi \boldsymbol{v}_\pi)}{\partial t} + \nabla \cdot (\rho_\pi \boldsymbol{v}_\pi \otimes \boldsymbol{v}_\pi), \tag{1}$$

where the subscripts $\pi = \mathrm{s}, \mathrm{f}$ denote the solid and fluid phase, respectively; ρ represents the density, $\boldsymbol{v}$ the absolute velocity, and $\boldsymbol{\sigma}$ the stress of the constituents. Furthermore, $\hat{\boldsymbol{p}}_\pi$ represents the momentum source from the other constituent, which accounts for the load drag between the solid

and fluid phase. For a closed system, the momentum source must fulfill the following:

$$\hat{\boldsymbol{p}}_s + \hat{\boldsymbol{p}}_f = 0. \tag{2}$$

Neglecting the body forces and inertia terms, Eq. (1) is reduced to

$$\nabla \cdot \boldsymbol{\sigma}_\pi + \hat{\boldsymbol{p}}_\pi = 0. \tag{3}$$

2.1.2 Mass balance

For a two-phase medium, the continuity equation is expressed by (Lewis & Schrefler, 1987):

$$\frac{\partial \rho_\pi}{\partial t} + \nabla \cdot (\rho_\pi \boldsymbol{v}_\pi) - \text{grad} \cdot \rho_\pi \cdot \boldsymbol{v}_\pi = 0, \tag{4}$$

where ρ is the mass density and $\boldsymbol{v}$ is the absolute velocity. The volume ratios of the solid and fluid phases n_s and n_f, respectively, must fulfill the following equation:

$$n_\text{s} + n_\text{f} = 1. \tag{5}$$

The apparent mass density for each constituent is obtained by

$$\rho_\pi = n_\pi \times \bar{\rho}_\pi, \tag{6}$$

where $\bar{\rho}$ is the absolute mass density. Substituting Eq. (6) into Eq. (4) yields:

$$n_\text{s} \nabla \cdot \boldsymbol{v}_\text{s} + \frac{1}{\bar{\rho}_\text{s}} \frac{\partial \rho_\text{s}}{\partial t} = 0, \tag{7}$$

$$n_\text{f} \nabla \cdot \boldsymbol{v}_\text{f} + \frac{1}{\bar{\rho}_\text{f}} \frac{\partial \rho_\text{f}}{\partial t} = 0. \tag{8}$$

Combining Eq. (5) with Eqs. (7) and (8) results in:

$$\nabla \cdot \boldsymbol{v}_\text{s} + n_\text{f} \nabla \cdot (\boldsymbol{v}_\text{f} - \boldsymbol{v}_\text{s}) + \frac{1}{\rho_\text{s}} \frac{\partial \rho_\text{s}}{\partial t} + \frac{1}{\rho_\text{f}} \frac{\partial \rho_\text{f}}{\partial t} = 0. \tag{9}$$

For a compressible solid, the time derivative of the solid phase density is obtained from the mass conservation equation (Lewis & Schrefler, 1987):

$$\frac{\partial (\rho_\text{s} \boldsymbol{v}_\text{s})}{\partial t} = 0. \tag{10}$$

From the entropy inequality (Hassanizadeh & Gray, 1990) for unsaturated flow accounting for the interfaces, the pressure in the solid phase is:

$$p_\text{s} = p_\text{f} \times n_\text{f}. \tag{11}$$

Assuming that the solid density is a function of the pressure p_s and temperature yields the following:

$$\frac{1}{\rho_\text{s}} \frac{\partial \rho_\text{s}}{\partial t} = -\frac{1}{\boldsymbol{v}_\text{s}} \frac{\partial \boldsymbol{v}_\text{s}}{\partial t} = \frac{1}{K_\text{s}} \frac{\partial p_\text{s}}{\partial t} + \beta_\text{s} \frac{\partial T_\text{s}}{\partial t}, \tag{12}$$

where K_s designates the solid phase bulk modulus, β_s is the thermal expansion coefficient, and T_s is the temperature. As the entire process takes place under isothermal conditions, the final item can be omitted:

$$\frac{1}{\rho_\text{s}} \frac{\partial \rho_\text{s}}{\partial t} = -\frac{1}{\boldsymbol{v}_\text{s}} \frac{\partial \boldsymbol{v}_\text{s}}{\partial t} = \frac{1}{K_\text{s}} \frac{\partial p_\text{s}}{\partial t}. \tag{13}$$

We define the Biot constant (Lewis & Schrefler, 1987) as

$$1 - \alpha = \frac{K_\text{T}}{K_\text{s}}, \tag{14}$$

where K_T is the overall bulk modulus of the two-phase medium and α is the Biot coefficient. The change in the solid mass density is related to its volume change by

$$\nabla \cdot \boldsymbol{v}_\text{s} = -\frac{K_\text{s}}{K_\text{T}} \frac{n_\text{s}}{\rho_\text{s}} \frac{\partial \rho_\text{s}}{\partial t}. \tag{15}$$

Substituting Eq. (14) into Eq. (15) results in

$$(1 - \alpha) \nabla \cdot \boldsymbol{v}_\text{s} = \frac{n_\text{s}}{\rho_\text{s}} \frac{\partial \rho_\text{s}}{\partial t}. \tag{16}$$

For the fluid phase, the relationship between the incremental change in fluid density and fluid pressure is expressed as:

$$\frac{1}{Q} \mathrm{d}p = \frac{n_\text{f}}{\rho_\text{f}} \mathrm{d}p_\text{f}, \tag{17}$$

with the compressibility modulus

$$\frac{1}{Q} = \frac{\alpha - n_\text{f}}{K_\text{s}} + \frac{n_\text{f}}{K_\text{f}}, \tag{18}$$

where K_f is the fluid phase bulk modulus. Inserting Eqs. (17) and (18) into Eq. (9) yields the mass balance equation:

$$\alpha \nabla \cdot \boldsymbol{v}_\text{s} + n_\text{f} \nabla \cdot (\boldsymbol{v}_\text{f} - \boldsymbol{v}_\text{s}) + \frac{1}{Q} \frac{\partial p}{\partial t} = 0. \tag{19}$$

2.1.3 Kinematic relation

Assuming a linear elastic solid, the kinematic relation for the small strain theory is expressed as:

$$\epsilon_\text{s} = \nabla^s \boldsymbol{u}_\text{s}, \tag{20}$$

where ϵ_s and $\boldsymbol{u}_\text{s}$ are the linear strain tensor and displacement field, respectively, of the solid phase.

2.1.4 Constitutive relation

The effective stress increment $\mathrm{d}\boldsymbol{\sigma}'_\text{s}$ in the solid is expressed as:

$$\mathrm{d}\boldsymbol{\sigma}'_\text{s} = \frac{\mathrm{d}\boldsymbol{\sigma}_\text{s}}{n_\text{s}}. \tag{21}$$

The incremental stress-strain relationship for the solid media is:

$$\mathrm{d}\boldsymbol{\sigma}_\text{s} = \boldsymbol{D} : \mathrm{d}\boldsymbol{\epsilon}_\text{s}, \tag{22}$$

where $\boldsymbol{D}$ is the fourth-order elasticity tensor.

2.2 Boundary conditions

The boundary conditions for the two-phase media (see Fig. 2) are expressed by

$$\boldsymbol{n}_\Gamma \cdot \boldsymbol{\sigma} = \boldsymbol{t}_\text{p} \quad \text{on } \partial\Omega_\text{t}; \quad \boldsymbol{u} = \boldsymbol{u}_\text{p} \quad \text{on } \partial\Omega_\text{u}, \tag{23}$$

where the von Neumann and Dirichlet boundaries $\partial\Omega_\text{t}$, $\partial\Omega_\text{u}$, and $\partial\Omega = \partial\Omega_\text{t} \cup \partial\Omega_\text{u}$, while $\boldsymbol{t}_\text{p}$ and $\boldsymbol{u}_\text{p}$ describe the traction and displacement, respectively. According to

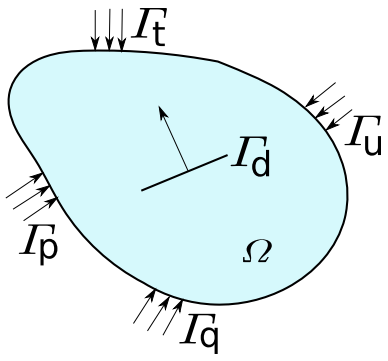

Fig. 2. Schematic illustration of boundary conditions.

Darcy's law (Darcy 1856) for isotropic media, the fluid velocity ($\boldsymbol{v}$) is related to the Darcy flux ($\boldsymbol{q}$) by the porosity (ϕ).

$$\phi \boldsymbol{v} = \boldsymbol{q} \tag{24}$$

On the complementary part of the boundary, $\partial\Omega_q$ and $\partial\Omega_p$, with $\partial\Omega = \partial\Omega_q \cup \partial\Omega_p$, hold:

$$n_f(\boldsymbol{v}_f - \boldsymbol{v}_s)\cdot n_\Gamma = \boldsymbol{q}_p \cdot n_\Gamma \ \text{ on } \partial\Omega_q; \quad p = p_p \ \text{ on } \partial\Omega_p, \tag{25}$$

where $\boldsymbol{q}_p \cdot n_\Gamma$ and p describe the outflow of the pore fluid and pressure, respectively.

2.3 Weak form and coupling

In order to derive the weak form from the strong form, we multiply the momentum balance equation (3) and mass balance equation (19) with kinematically admissible test functions for the displacements and pressure. Integrating by parts and the Gauss divergence theorem, and applying Darcy's law, finally leads to the well-known weak form:

$$\int_\Omega (\nabla\cdot\boldsymbol{\eta})\cdot\boldsymbol{\sigma}\,d\Omega + \boxed{\int_{\Gamma_d} [\![\boldsymbol{\eta}]\!]\cdot\boldsymbol{\sigma}\cdot\boldsymbol{n}_{\Gamma_d}\,d\Omega} = \int_\Gamma \boldsymbol{\eta}\cdot\boldsymbol{t}_p\,d\Omega \tag{26}$$

$$-\int_\Omega \alpha\,\xi\nabla\cdot\boldsymbol{v}_s\,d\Omega + \int_\Omega k_f\nabla\xi\cdot\nabla p\,d\Omega - \int_\Omega \xi\,Q^{-1}\dot{p}\,d\Omega + \boxed{\int_{\Gamma_d} \boldsymbol{n}_{\Gamma_d}\cdot[\![\xi n_f(\boldsymbol{v}_f - \boldsymbol{v}_s)]\!]\,d\Gamma} = \int_\Gamma \xi\,\boldsymbol{n}_\Gamma\cdot\boldsymbol{q}_p\,d\Omega\,, \tag{27}$$

where $\dot{p} = \frac{\partial p}{\partial t}$ denotes the time derivatives. The traction force on Γ_d is induced by the flow pressure inside the cavity. Owing to the presence of discontinuity inside the domain, the traction force $\boldsymbol{\sigma}\cdot\boldsymbol{n}_{\Gamma_d}$ on Γ_d and fluid flux $[\![\xi n_f(\boldsymbol{v}_f - \boldsymbol{v}_s)]\!]$ through the discontinuity face are essential parts of the weak form. As the cavity length-to-width ratio is considerably large, one could assume that the traction forces on each side of the cavity are equal. Because of the continuity from the bulk to the cavity, this yields

$$\boldsymbol{\sigma}\cdot\boldsymbol{n}_{\Gamma_d} = -p\boldsymbol{n}_{\Gamma_d} \ \text{ on } \Gamma_d. \tag{28}$$

Substituting Eq. (28) into Eq. (26), the final weak form of the momentum balance equation is expressed by

$$\int_\Omega (\nabla\cdot\boldsymbol{\eta})\cdot\boldsymbol{\sigma}\,d\Omega - \int_{\Gamma_d} [\![\eta]\!]\cdot p\boldsymbol{n}_{\Gamma_d}\,d\Omega = \int_\Gamma \boldsymbol{\eta}\cdot\boldsymbol{t}_p\,d\Omega. \tag{29}$$

Darcy's law is expressed by

$$\boldsymbol{v} = \frac{\boldsymbol{q}}{\phi}, \tag{30}$$

where ϕ is the bulk porosity and $\boldsymbol{v} = \boldsymbol{v}_f - \boldsymbol{v}_s$ is the velocity. The pressure values for both cavity faces are identical, which leads to the following coupling term of the weak form for the mass balance equation:

$$\int_{\Gamma_d} \boldsymbol{n}_{\Gamma_d}\cdot[\![\xi n_f(\boldsymbol{v}_f - \boldsymbol{v}_s)]\!]\,d\Gamma = \int_{\Gamma_d} \xi n_f \boldsymbol{n}_{\Gamma_d}\cdot[\![\boldsymbol{v}_f - \boldsymbol{v}_s]\!]\,d\Gamma = \int_{\Gamma_d} \xi\boldsymbol{n}_{\Gamma_d}\cdot\boldsymbol{q}_d\,d\Gamma, \tag{31}$$

where $\boldsymbol{q}_d$ is the flow flux through the discontinuity.

2.4 Fluid flow inside cavity

Assuming that the fluid flow inside the cavity is a Newtonian fluid, the general momentum balance equation reads as follows (Bachelor 1967):

$$\underbrace{\frac{\partial \boldsymbol{u}}{\partial t}}_{\text{Variation}} + \underbrace{(\boldsymbol{u}\cdot\nabla)\boldsymbol{u}}_{\text{Convection}} - \underbrace{\mu\nabla^2\boldsymbol{u}}_{\text{Diffusion}} = \underbrace{-\nabla w}_{\text{Internal source}} + \underbrace{g}_{\text{External source}}, \tag{32}$$

where μ is the fluid viscosity and $\boldsymbol{u}$ is the fluid velocity.

Assuming small displacements and no mass exchange, and neglecting the body and inertia forces, the momentum balance equation is simplified to:

$$\underbrace{-\mu\nabla^2\boldsymbol{u}}_{\text{Diffusion}} = \underbrace{-\nabla w}_{\text{Internal source}}. \tag{33}$$

In the two-phase medium, the interface pressure on the two sides of the cavity serves as an internal momentum source, which results in the final momentum balance equation:

$$\mu\nabla^2\boldsymbol{v}_{\bar{f}} = \nabla p, \tag{34}$$

where $\boldsymbol{v}_{\bar{f}}$ denotes the fluid flow velocity and the subscript $\bar{f}$ denotes the fluid inside the cavity.

Owing to the high length-to-cross-section ratio (Fig. 3), the fluid flow inside the cavity can be considered as a quasi 1D flow, expressed by

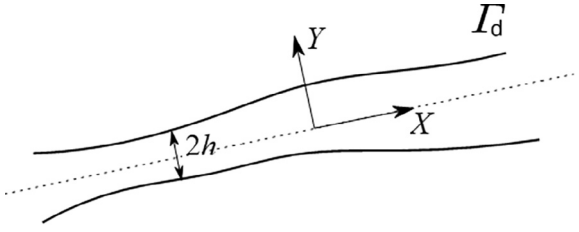

Fig. 3. Schematic illustration of cavity geometry.

$$\frac{\partial p_{\bar{f}}}{\partial \bar{y}} = 0 \tag{35}$$

in the normal direction $\boldsymbol{n}_{\Gamma_d}$, and in the tangential direction of $\boldsymbol{t}_{\Gamma_d}$:

$$\frac{\partial p_{\bar{f}}}{\partial \bar{x}} = \mu \frac{\partial^2 v_{\bar{f}}}{\partial \bar{y}^2}, \tag{36}$$

where $\bar{x}$ and $\bar{y}$ are coordinates with respect to the normal and tangent cavity directions, respectively. In the normal direction $\boldsymbol{n}_{\Gamma_d}$ of the cavity, the pressure $p_{\bar{f}}$ is constant through the cavity cross-section; for continuity restriction, $p_{\bar{f}}$ must be equal to p.

$$p_{\bar{f}} = p. \tag{37}$$

In order to derive the axial velocity, Eq. (36) is integrated twice with regard to the y-coordinate:

$$\int_{-h}^{h}\int_{-h}^{h} \frac{\partial p}{\partial \bar{x}} = \int_{-h}^{h}\int_{-h}^{h} \mu \frac{\partial^2 v_{\bar{f}}}{\partial \bar{y}^2}, \tag{38}$$

yielding

$$v(y) = \frac{1}{2\mu}\frac{\partial p}{\partial \bar{x}}(\bar{y}^2 - h^2) + v_f, \tag{39}$$

where $v_f = \boldsymbol{v}_f \cdot \boldsymbol{t}_{\Gamma_d}$ serves as the essential boundary condition on both sides of the cavity.Under the assumption of smaller concentration changes, the mass balance for fluid inside the cavity is expressed as:

$$\frac{\partial \rho}{\partial t} + \rho \nabla \cdot \boldsymbol{u}_{\bar{f}} = 0. \tag{40}$$

Assuming that the fluid inside the cavity is mono-phase (with no mass transfer between the cavity and bulk), the mass balance equation is simplified to

$$\nabla \cdot \boldsymbol{u}_{\bar{f}} = 0. \tag{41}$$

Obviously, the flow velocity inside the cavity is significantly higher than in the bulk. The mass balance equation can be rewritten:

$$\frac{\partial v}{\partial \bar{x}} + \frac{\partial w}{\partial \bar{y}} = 0, \tag{42}$$

where $w = \boldsymbol{v}_{\bar{f}} \cdot \boldsymbol{n}_{\Gamma_d}$ denotes the normal velocity of the fluid flow inside the cavity.

The mass balance equation is averaged over the cavity width:

$$\int_{-h}^{h} \frac{\partial v}{\partial \bar{x}} \mathrm{d}\bar{y} + \int_{-h}^{h} \frac{\partial w}{\partial \bar{y}} \mathrm{d}\bar{y} = 0. \tag{43}$$

The difference in the fluid flow between the two sides of the cavity is given by

$$[\![w_{\bar{f}}]\!] = w(h) - w(-h) = -\int_{-h}^{h} \frac{\partial v}{\partial \bar{x}} \mathrm{d}\bar{y}. \tag{44}$$

Substituting Eq. (39) into Eq. (44) yields:

$$[\![w_{\bar{f}}]\!] = \frac{2}{3\mu}\frac{\partial}{\partial \bar{x}}\left(\frac{\partial p}{\partial \bar{x}} h^3\right) - 2h\frac{\partial v_{\bar{f}}}{\partial \bar{x}}. \tag{45}$$

This equation describes the total amount of fluid attracted in the tangential flow. It can be included in the weak form for the mass coupling, which ensures coupling between the fluid inside the cavity and that in the bulk. Indeed, the coupling term $n_f \boldsymbol{n}_{\Gamma_d} \cdot [\![v_f - v_s]\!]$ can be expressed as:

$$\begin{aligned} n_f \boldsymbol{n}_{\Gamma_d} \cdot [\![v_f - v_s]\!] &= n_f [\![w_{\bar{f}} - w_s]\!] \\ &= n_f \left(\frac{2}{3\mu}\frac{\partial}{\partial \bar{x}}\left(\frac{\partial p}{\partial \bar{x}} h^3\right) - 2h\frac{\partial v_f}{\partial \bar{x}} - 2\frac{\partial h}{\partial t}\right), \end{aligned} \tag{46}$$

where w_s is the normal velocity of the solid skeleton, and the difference between the two sides of the cavity gives:

$$w_s = 2\frac{\partial h}{\partial t}. \tag{47}$$

Following Darcy's law, the tangential velocity reads:

$$v_{\bar{f}} = \left(\boldsymbol{v}_s - \frac{k_f}{n_f}\nabla p\right) \cdot \boldsymbol{t}_{\Gamma_d}. \tag{48}$$

3 Discretization

3.1 Approximation of primary fields

The crack (or cavity) leads to a discontinuous displacement field, while the pressure field across the cavity is continuous. Moreover, the spatial derivatives of the pressure orthogonal to the cracks are also discontinuous. Hence, the displacement field discretization is expressed by

$$\begin{aligned} \boldsymbol{u}_s(x) = &\sum_{i\in N} N_i(x)\bar{\boldsymbol{u}}_i + \sum_{i\in N_{cut}} N_i(x)\aleph_{\Gamma_d}(x)\hat{\boldsymbol{u}}_i \\ &+ \sum_{i\in N_{tip}}\sum_{j\in[1,4]} N_i(x)\Psi_j(x)\tilde{u}_{ij}, \end{aligned} \tag{49}$$

where N_i are the standard finite element shape functions, and $\bar{u}_i$, $\hat{u}_i$, and $\hat{u}_i$ are the nodal parameters. Moreover, the Heaviside function is defined by

$$\aleph_{\Gamma_d}(x) = \begin{cases} 0 & \text{if } \phi(x) \leqslant 0 \\ 1 & \text{if } \phi(x) > 0 \end{cases}, \tag{50}$$

where $\phi(x)$ is the level-set function.

For the node set N_{tip}, we include the well-known crack tip enrichment functions in Ψ_j:

$$\psi_1(\boldsymbol{x}) = \sqrt{r}\sin\frac{\theta}{2}, \tag{51}$$

$$\psi_2(\boldsymbol{x}) = \sqrt{r}\sin\frac{\theta}{2}\sin\theta, \tag{52}$$

$$\psi_3(\boldsymbol{x}) = \sqrt{r}\cos\frac{\theta}{2}, \tag{53}$$

$$\psi_4(\boldsymbol{x}) = \sqrt{r}\cos\frac{\theta}{2}\sin\theta. \tag{54}$$

These functions depend on the local coordinate system (r, θ) illustrated in Fig. 4. Equation (49) can be rewritten as

$$\boldsymbol{u}_s = \boldsymbol{N}\boldsymbol{U}, \tag{55}$$

where the matrix $\boldsymbol{N}$ contains the standard and enriched shape functions. Accordingly, the array $\boldsymbol{U}$ includes the displacement for the standard and enriched degrees of freedom $\bar{u}_i, \hat{u}_i$, and $\tilde{u}_{ij}$.

For the pressure discretization, the node set N_{pres} is enriched with the signed distance function $\boldsymbol{D}_{\Gamma_d}$. The enriched distance function $\boldsymbol{D}_{\Gamma_d}$ is continuous to discontinuous, but its normal derivative is discontinuous.

$$D_{\Gamma_d}(x) = \begin{cases} -d & \text{if } \phi(x) \leqslant 0 \\ d & \text{if } \phi(x) > 0 \end{cases}, \tag{56}$$

where d is the absolute distance to the discontinuity.

The node set N_{pres} includes the nodes affected by the crack. Hence, the pressure field discretization can be expressed as

$$p(\boldsymbol{x}) = \sum_{i \in N} H_i(\boldsymbol{x})\bar{p}_i + \sum_{i \in N_{pres}} H_i(\boldsymbol{x})\boldsymbol{D}_{\Gamma_d}(\boldsymbol{x})\hat{p}_i, \tag{57}$$

where H_i is the standard FE shape function for the pressure. We can also rewrite this expression in matrix-vector form as

$$p = \boldsymbol{H}\boldsymbol{P}, \tag{58}$$

where $\boldsymbol{H}$ contains the standard and enriched shape functions, and $\boldsymbol{P}$ contains the degrees of freedom for the pressures $\bar{p}_i$ and $\hat{p}_i$. The order of the shape function N_i and H_i should be adequate for fulfilling the modeling requirements. For the consideration of the momentum balance equation consistency, the order of the displacement shape function N_i should be greater than or equal to that of the pressure shape function H_i. This study uses the quadrilateral elements equipped with linear shape functions.

4 Discrete equations

The vectors of the external force $\boldsymbol{F}_{\text{ext}}$ and external fluid flux $\boldsymbol{Q}_{\text{ext}}$ are given by:

$$\boldsymbol{F}_{\text{ext}} = \int_{\Gamma} \boldsymbol{N}^{\text{T}} \boldsymbol{t}_{\text{p}} \mathrm{d}\Gamma, \tag{59}$$

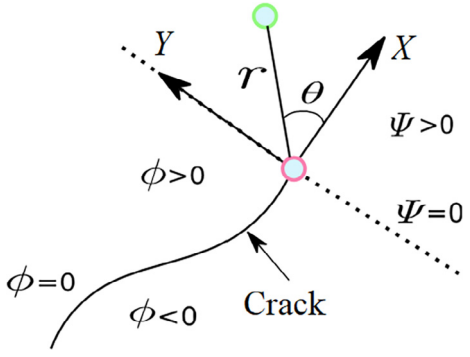

Fig. 4. Local coordinates (r, θ) at tip element.

$$\boldsymbol{Q}_{\text{ext}} = \int_{\Gamma} \boldsymbol{H}^{\text{T}} \boldsymbol{n}_{\text{t}} \boldsymbol{q}_{\text{p}} \mathrm{d}\Gamma. \tag{60}$$

Using backward finite difference approximation:ṡ

$$\left(\frac{\partial \cdot}{\partial t}\right)_i = \frac{\cdot_i - \cdot_{i-1}}{\Delta t}, \tag{61}$$

where Δx is the time increment, and $\cdot_i$ and $\cdot_{i-1}$ denote the unknowns at time steps i and $i-1$, respectively.

The coupling force vector $F_{coupling}$ (on the crack boundary) is derived from Eq. (29):

$$F_{\text{coupling}} = -\left(\int_{\Gamma_d} [\![\eta]\!]^{\text{T}} \boldsymbol{n}_{\Gamma_d} \boldsymbol{H}\right) \boldsymbol{P}. \tag{62}$$

Integrating Eq. (31) along Γ_d yields the internal fluid flux $Q_{coupling}$:

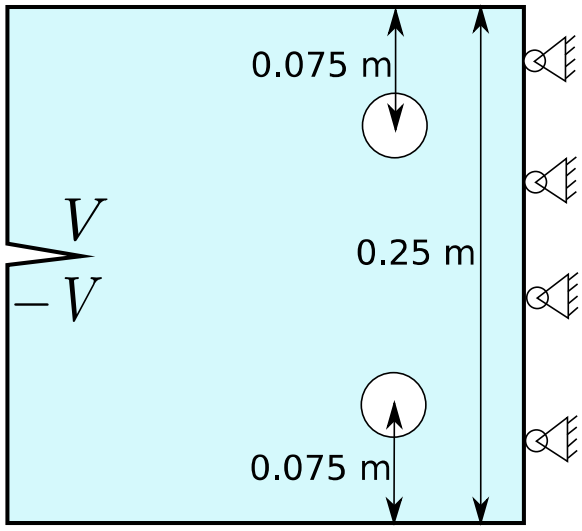

(a) Geometry and boundary condition

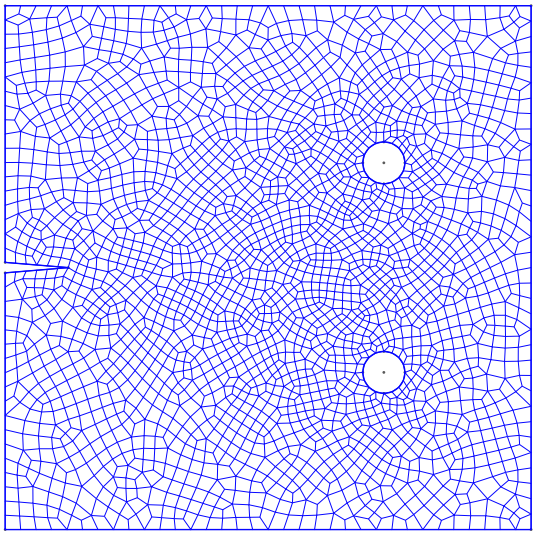

(b) Mesh configuration

Fig. 5. (a) Domain geometry and boundary condition of the example; and (b) mesh configuration of the example.

$$Q_{\text{coupling}} = \int_{\Gamma_d} \boldsymbol{H}^{\mathrm{T}} \boldsymbol{n}_{\Gamma_d}^{\mathrm{T}} \boldsymbol{q}_d \mathrm{d}\Gamma_d. \tag{63}$$

The internal fluid flux Q_{coupling} formation is nonlinear; hence, an iteration procedure must be conducted at each time step Δt in order to control the resolution accuracy. The iteration residual vector $\boldsymbol{R}^i$ at thei_{th} iteration is defined as:

$$\boldsymbol{R}^i = \begin{bmatrix} 0 & 0 \\ \boldsymbol{K}_{\text{up}}^{\mathrm{T}} & \boldsymbol{K}_{\text{pp}}^{(1)} \end{bmatrix} \begin{pmatrix} \Delta U \\ \Delta P \end{pmatrix}^i + \begin{bmatrix} \boldsymbol{K}_{\text{uu}} & \boldsymbol{K}_{\text{up}} \\ 0 & \Delta t \boldsymbol{K}_{\text{pp}}^{(2)} \end{bmatrix} \begin{pmatrix} U \\ P \end{pmatrix}^i + \begin{pmatrix} F_{\text{coupling}} \\ Q_{\text{coupling}} \end{pmatrix}^i - \begin{pmatrix} F_{\text{ext}} \\ Q_{\text{ext}} \end{pmatrix}, \tag{64}$$

with the following stiffness matrix:

$$\boldsymbol{K}_{\text{uu}} = \int_\Omega \boldsymbol{B}^{\mathrm{T}} \boldsymbol{D}^{tan} \boldsymbol{B} \mathrm{d}\Omega \tag{65}$$

$$\boldsymbol{K}_{\text{up}} = -\int_\Omega \alpha \boldsymbol{B}^{\mathrm{T}} \boldsymbol{m} \boldsymbol{H} \mathrm{d}\Omega \tag{66}$$

$$\boldsymbol{K}_{\text{pp}}^{(1)} = -\int_\Omega Q^{-1} \boldsymbol{H}^{\mathrm{T}} \boldsymbol{H} \mathrm{d}\Omega \tag{67}$$

Table 1
Material properties.

Name	Symbol	Value
Fluid volume fraction	n_{f}	0.3
Density (solid)	ρ_{s}	2 000 kg/m^3
Density (fluid)	ρ_{f}	1 000 kg/m^3
Young's modulus	E	5 GPa
Poisson ratio	v	0.4
Fluid dynamic viscosity	μ_{w}	10^{-3} N/m^2
Biot modulus	Q	10^{18} GPa
Fluid viscosity	μ	10^{-3}N/(m$^2 \cdot$ s)

$$\boldsymbol{K}_{\text{pp}}^{(2)} = -\int_\Omega k_f \nabla \boldsymbol{H}^{\mathrm{T}} \nabla \boldsymbol{H} \mathrm{d}\Omega, \tag{68}$$

where $\boldsymbol{m} = [1, 1, 0]$ for a 2D problem.

In the Newtown-Raphson algorithm, the iteration matrix $\boldsymbol{K}^i$ is derived from:

$$\boldsymbol{K}^i = \frac{\partial f}{\partial \cdot}, \tag{69}$$

where f and • denote the residual function and unknowns, respectively. In this study, the iteration matrix $\boldsymbol{K}^i$ takes the following form:

$$\boldsymbol{K}^i = \begin{bmatrix} \boldsymbol{K}_{\text{uu}} & \boldsymbol{K}_{\text{up}} + \frac{\partial F_{\text{coupling}}}{\partial P} \\ \boldsymbol{K}_{\text{up}}^{\mathrm{T}} + \Delta t \frac{\partial Q_{\text{coupling}}}{\partial U} & \boldsymbol{K}_{\text{pp}}^{(1)} + \Delta t \boldsymbol{K}_{\text{pp}}^{(2)} + \frac{\partial Q_{\text{coupling}}}{\partial P} \end{bmatrix}, \tag{70}$$

where all items are evaluated at iteration i.

The coupling terms $\boldsymbol{F}_{\text{coupling}}$ and $\boldsymbol{Q}_{\text{coupling}}$ cause the Jacobian matrix of the residual $\boldsymbol{R}^i$ to become asymmetric; in order to regain the symmetry, the coupling terms are omitted in the Jacobian matrix. This may decrease the convergence rate of the Newton–Raphson algorithm. However, the symmetric matrix allows for flexible implementation as well as an improved condition of the matrix structure. The simplified Jacobian matrix is expressed as:

$$\boldsymbol{K}^i = \begin{bmatrix} \boldsymbol{K}_{\text{uu}} & \boldsymbol{K}_{\text{up}} + \frac{\partial F_{\text{coupling}}}{\partial P} \\ \boldsymbol{K}_{\text{up}}^{\mathrm{T}} & \boldsymbol{K}_{\text{pp}}^{(1)} + \Delta t \boldsymbol{K}_{\text{pp}}^{(2)} \end{bmatrix}. \tag{71}$$

5 Example calculation

In this section, we present an example based on the experimental setup of (Bruno & Nakagawa, 1991). Figure 5 illustrates the boundary conditions, geometries, and mesh configuration of the studied sample. Details regarding the example are presented in the following paragraphs.

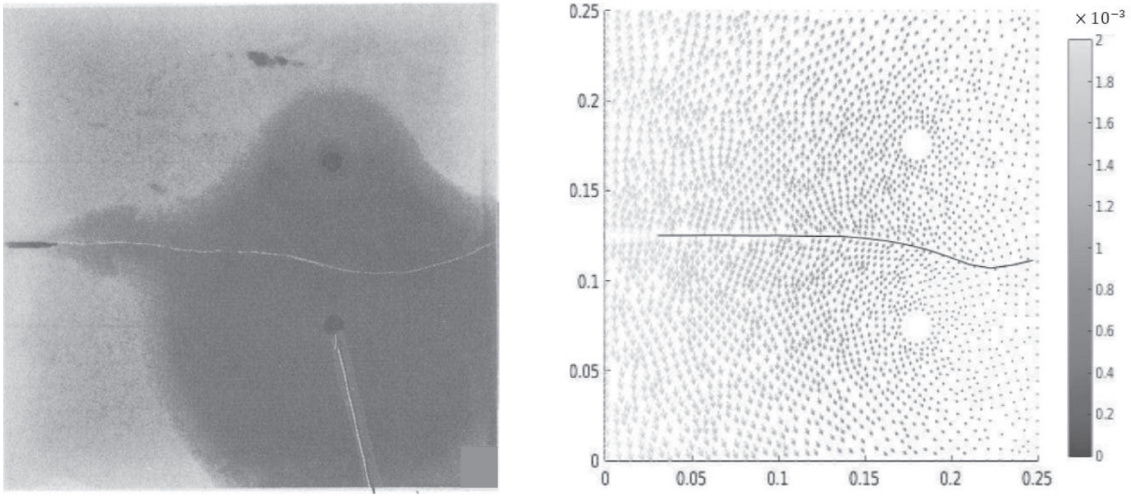

(a) Experiment results (Bruno and Nakagawa 1991) (b) Simulation results

Fig. 6. Crack propagation path.

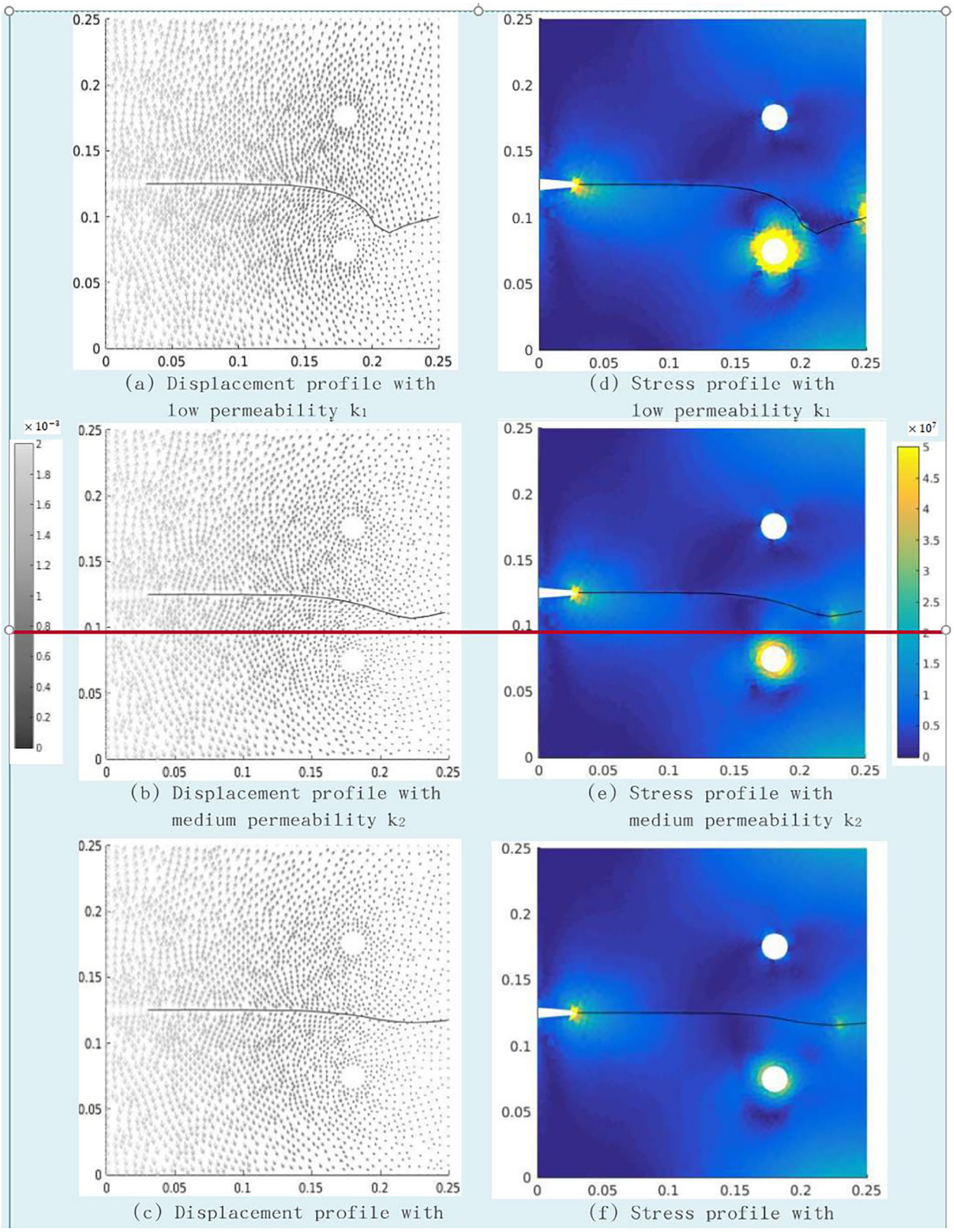

Fig. 7. Displacement (m) plot of porous media with intrinsic permeabilities: (a) $k1 = 2.78 \times 10^{-18}$ m^2; (b) $k2 = 1.52 \times 10^{-17}$ m^2; (c) $k3 = 2.78 \times 10^{-17}$ m^2 and (d) to (f): stress (Pa) plots in cylinder coordinates.

Bruno and Nakagawa (Bruno & Nakagawa, 1991) conducted an experiment to demonstrate the tensile fracture propagation path influenced by pore pressure in sedimentary rock. Their experimental setup can be summarized as follows. A square sample (Fig. 5) with two ports and high pore pressure is introduced to the lower port region

by injecting pressurized fluid and the pressure is maintained. Hereafter, a wedge is driven into the pre-shaped concave edge to induce fracturing and fracture propagation, following which the crack propagation path is identified. We reproduce this exact experimental setup with the presented model. The difference between our numerical setup and the original experiment is that displacement velocities are applied to the concave surface in our model, instead of a driving wedge, which requires modeling a solid-to-solid contact effect that is beyond the scope this manuscript. Based on the experimental setup, the material parameters used in the presented model are listed in Table 1. Furthermore, three different intrinsic porous media permeabilities are selected ($k_1 = 2.78 \times 10^{-18}\,\mathrm{m}^2$; $k_2 = 1.52 \times 10^{-17}\,\mathrm{m}^2$; $k_3 = 2.78 \times 10^{-17}\,\mathrm{m}^2$) to study its impact on the crack propagation path. The injection fluid flux $Q_{\mathrm{in}} = 10^{-4}\mathrm{m/s}$ is applied at a lower port and maintained during the simulation. Opposite displacement velocities $V = 10^{-4}\,\mathrm{m/s}$ and $-V = -10^{-4}\,\mathrm{m/s}$ are applied on the upper and lower edges of the concave surface, respectively. The simulation ends when the propagated crack reaches the opposite boundary. Figure 6 illustrates the crack propagation path from the experimental and numerical simulations. It is clearly indicated that the present model exhibits strong agreement with the experiment in terms of the crack propagation path, and the model is capable of predicting the crack propagation direction even under the influence of existing pore pressure. The fracture development path, domain displacement, and stress profiles are displayed in Fig. 7 for porous medias (under identical loading) with different intrinsic permeabilities (k_1, k_2, k_3). Figure 7(d)–(f) clearly demonstrate that the fracture paths are attracted to the fluid-pressurized port. Furthermore, under identical injection rates, porous media with a lower permeability (e.g. k_1) will induce a higher stress/pressure state around the injection port compared to porous media with a higher permeability (e.g. k_3), which in turn influences the fracture propagation direction.

6 Conclusion

In this study, we present an XFEM for hydraulic fracture under the influence of pressurized voids. The crack is described by the level-set method, and an abs-enrichment is adopted to describe the discontinuous pressure field. The fluid phase is assumed as an incompressible Newtonian fluid, whereas the solid phase is assumed as isotropic and linear-elastic. The nonlinear equation is solved by means of the Newton–Raphson method with a backward integration scheme. The numerical examples in this study are based on and validated by an experimental setup. We observe that the fracture propagation path is attracted to the pressurized zone, and the essential properties (such as permeability) of the porous media have a significant impact on the fracture propagation direction. This study demonstrates that the presented model is capable of capturing the fracture propagation path under existing fluid pressure, and suggests that, during the hydraulic fracture process, it is essential to consider the geographical conditions.

Acknowledgments

The authors gratefully acknowledge the support received from the NSFC Program (51474157), State Key Laboratory for Geomechanics and Deep Underground Engineering, China University of Mining & Technology (SKLGDUEK1526), Science and Technology Commission of Shanghai Municipality (16QA1404000), and Fundamental Research Funds for the Central Universities.

Conflict of interest

The authors have no interest conflict to declare.

Appendix A Crack propagation criteria

Consider an arbitrary counterclockwise path (Γ) around the crack tip part. The well-known path-independent J-integral (Cherepanov 1979) is expressed by:

$$J = \int_{\Gamma} \left(w\mathrm{d}y - T_i \frac{\partial u_i}{\partial x} \mathrm{d}s \right), \tag{A.1}$$

where

w = strain energy density;
T_i = traction vector components;
u_i = displacement vector components;
ds = length increment along contour Γ.

The strain energy density is

$$w = \int_0^{\epsilon_{ij}} \sigma_{ij} \mathrm{d}\epsilon_{ij}, \tag{A.2}$$

where ϵ_{ij} and $\boldsymbol{\sigma}_{ij}$ are the strain and stress tensors, respectively. The traction vector components are given by

$$T_i = \sigma_{ij} n_j. \tag{A.3}$$

The J-integral coincides with the energy release rate G at the crack tip; that is, $G = J$, for isotropic material under plain-strain conditions. The energy release rate is related to the stress intensity factors by

$$G = \left(K_{\mathrm{IC}}^2 + K_{\mathrm{IC}}^2\right)\left(\frac{1-\nu^2}{E}\right), \tag{A.4}$$

where I and II represent models I and II, respectively, v is the Poisson ratio, and E is the Young's modulus.

In order to extract the individual stress intensity factors K_{I} and K_{II}, we consider two states: state 1 corresponds to the actual state of interest, while state 2 is an auxiliary state serving as the asymptotic field for models I and II.

The J_{d} integral for the sum of the two states is as follows:

$$J^{(1+2)} = J^{(1)} + J^{(2)} + M^{(1+2)}, \tag{A.5}$$

where M is the interaction integral of the two states.

$$M^{(1+2)} = \int_A \left[\left(W^{(1,2)} \mathrm{d}y - T_i^{(1)} \frac{\partial u_i^{(2)}}{\partial x} + T_i^{(2)} \frac{\partial u_i^{(1)}}{\partial x} \right) \right] \mathrm{d}s, \tag{A.6}$$

where $W^{(1,2)}$ is the interaction strain energy.

$$W^{(1,2)} = T_i^{(1)} \frac{\partial u_i^{(2)}}{\partial x} = T_i^{(2)} \frac{\partial u_i^{(1)}}{\partial x} \tag{A.7}$$

Combining the relationships $= J$, $G^{(1+2)} = G^{(1)} + G^{(2)}$, and Eqs. (A.5) and (A.6), the interaction integral of the two states gives:

$$M^{(1+2)} = \frac{2(1-\nu^2)}{E} \left(K_{\mathrm{I}}^{(1)} K_{\mathrm{I}}^{(2)} + K_{\mathrm{II}}^{(1)} K_{\mathrm{II}}^{(2)} \right). \tag{A.8}$$

The stress intensity factor of the actual state of model I is:

$$K_I^{(1)} = \frac{E}{2(1-\nu^2)} M^{(1,\text{model I})}, \tag{A.9}$$

with the auxiliary state as the model I asymptotic field $(K_{\mathrm{I}}^{(2)} = 1, K_{\mathrm{II}}^{(2)} = 0)$.

The stress intensity factor of the actual state of model II is:

$$K_{(\mathrm{II})}^{(1)} = \frac{E}{2(1-\nu^2)} M^{(1,\text{model II})}, \tag{A.10}$$

with the auxiliary state as the model II asymptotic field $(K_{\mathrm{I}}^{(2)} = 0, K_{\mathrm{II}}^{(2)} = I)$.

The effective stress intensity factor for a mixed-model crack propagation situation is expressed as:

$$K_{\mathrm{eff}}(\theta) = K_{\mathrm{I}} \cos^3\left(\frac{1}{2}\theta\right) - 3K_{\mathrm{II}} \sin\left(\frac{1}{2}\theta\right) \cos^2\left(\frac{1}{2}\theta\right). \tag{A.11}$$

It is postulated that crack growth will occur when

$$\max K_{\mathrm{eff}}(\theta) = K_{\mathrm{Cri}}, \tag{A.12}$$

with K_{Cri} as the critical stress intensity factor.

The direction of the propagation is given by the angle θ^K, which maximizes $K_{\mathrm{eff}}(\theta)$:

$$\theta^K = 2\arctan\left(\frac{K_{\mathrm{I}} - \sqrt{K_{\mathrm{I}}^2 + 8K_{\mathrm{II}}^2}}{4K_{\mathrm{II}}} \right). \tag{A.13}$$

Inserting Eq. (A.13) into Eq. (A.11), we obtain

$$\frac{4\sqrt{2}K_{\mathrm{II}}^3 \left(K_{\mathrm{I}} + 3\sqrt{K_{\mathrm{I}}^2 + 8K_{\mathrm{II}}^2} \right)}{\left(K_{\mathrm{I}}^2 + 12K_{\mathrm{II}}^2 - K_{\mathrm{I}}\sqrt{K_{\mathrm{I}}^2 + 8K_{\mathrm{II}}^2} \right)^{\frac{3}{2}}} = K_{\mathrm{Cri}}. \tag{A.14}$$

References

Abellan, M. A., & Borst, R. D. (2006). Wave propagation and localisation in a softening two-phase medium. *Computer Methods in Applied Mechanics and Engineering, 195*(37), 5011–5019.

Amiri, F., Anitescu, C., Arroyo, M., Bordas, S. P. A., & Rabczuk, T. (2014). XLME interpolants, a seamless bridge between XFEM and enriched meshless methods. *Computational Mechanics, 53*(1), 45–57.

Areias, P., Dias-da-Costa, D., Sargado, J. M., & Rabczuk, T. (2013a). Element-wise algorithm for modeling ductile fracture with the rousselier yield function. *Computational Mechanics, 52*(6), 1429–1443.

Areias, P., & Rabczuk, T. (2013b). Finite strain fracture of plates and shells with configurational forces and edge rotations. *International Journal for Numerical Methods in Engineering, 94*(12), 1099–1122.

Areias, P., Rabczuk, T., & Camanho, P. P. (2014). Finite strain fracture of 2D problems with injected anisotropic softening elements. *Theoretical and Applied Fracture Mechanics, 72*, 50–63.

Areias, P., Msekh, M. A., & Rabczuk, T. (2016). Damage and fracture algorithm using the screened poisson equation and local remeshing. *Engineering Fracture Mechanics, 158*, 116–143.

Areias, P., Rabczuk, T., & Camanho, P. P. (2013c). Initially rigid cohesive laws and fracture based on edge rotations. *Computational Mechanics, 52*(4), 931–947.

Areias, P., Rabczuk, T., & DiasdaCosta, D. (2013d). Element-wise fracture algorithm based on rotation of edges. *Engineering Fracture Mechanics, 110*, 113–137.

Bachelor, G. K. (1967). *An introduction to fluid mechanics*. Cambridge, UK: Cambridge University Press.

Bazant, Z. P. (1984). Size effect in blunt fracture: concrete, rock, metal. *Journal of Engineering Mechanics, 110*(4), 518–535.

Belytschko, T., & Black, T. (1999). Elastic crack growth in finite elements with minimal remeshing. *International Journal for Numerical Methods in Engineering, 45*(5), 601–620.

Belytschko, T., Guo, Y., Kam Liu, W., & Ping Xiao, S. (2000). A unified stability analysis of meshless particle methods. *International Journal for Numerical Methods in Engineering, 48*(9), 1359–1400.

Belytschko, T., Krongauz, Y., Organ, D., Fleming, M., & Krysl, P. (1996). Meshless methods: An overview and recent developments. *Computer Methods in Applied Mechanics and Engineering, 139*(1–4), 3–47.

Belytschko, T., & Tabbara, M. (1996). DYNAMIC fracture using element-free galerkin methods. *International Journal for Numerical Methods in Engineering, 39*(6), 923–938.

Bordas, S., Rabczuk, T., & Zi, G. (2008). Three-dimensional crack initiation, propagation, branching and junction in non-linear materials by an extended meshfree method without asymptotic enrichment. *Engineering Fracture Mechanics, 75*(5), 943–960.

Bruno, M. S., & Nakagawa, F. M. (1991). Pore pressure influence on tensile fracture propagation in sedimentary rock. *International Journal of Rock Mechanics and Mining Sciences & Geomechanics Abstracts, 28*, 261–273.

Chau-Dinh, T., Zi, G., Lee, P. S., Rabczuk, T., & Song, J. H. (2012). Phantom-node method for shell models with arbitrary cracks. *Computers & Structures, 92*(3), 242–256.

Cherepanov, G. P. (1979). *Mechanics of brittle fracture*. New York: McGraw-Hill.

Darcy, H. (1856). *Les Fontaines Publiques de La Ville de Dijon: Exposition et Application*. Paris: Hachette Livre Bnf.

Dolbow, J., & Belytschko, T. (1999a). A finite element method for crack growth without remeshing. *International Journal for Numerical Methods in Engineering, 46*(1), 131–150.

Dolbow, J., & Belytschko, T. (1999b). Numerical integration of the Galerkin weak form in meshfree methods. *Computational Mechanics, 23*(3), 219–230.

Gale, J. F. W., Reed, R. M., & Holder, J. (2007). Natural fractures in the Barnett Shale and their importance for hydraulic fracture treatments. *American Association of Petroleum Geologists (AAPG), 91*(4), 603–622.

Gerstenbergera, A., & Wall, W. A. (2008). An eXtended finite element method/lagrange multiplier based approach for fluid–structure interaction. *Computer Methods in Applied Mechanics and Engineering, 197*(19), 1699–1714.

Hansbo, A., & Hansbo, P. (2004). A finite element method for the simulation of strong and weak discontinuities in solid mechanics. *Computer Methods in Applied Mechanics and Engineering, 193*(33), 3523–3540.

Hassanizadeh, S. M., & Gray, W. G. (1990). Mechanics and thermodynamics of multiphase flow in porous media including interphase boundaries. *Advances in Water Resources, 13*(4), 169–186.

Lewis, R. W., & Schrefler, B. A. (1987). *The Finite Element Method in the Deformation and Consolidation of Porous Media*. New York, NY: John Wiley; Sons Inc.

Miehe, C., Welschinger, F., & Hofacker, M. (2010). Thermodynamically consistent phase-field models of fracture: Variational principles and multi-field FE implementations. *International Journal for Numerical Methods in Engineering, 83*(10), 1273–1311.

Nguyen, V. P., Rabczuk, T., Bordas, S., & Duflot, M. (2008). Meshless methods: A review and computer implementation aspects. *Mathematics and Computers in Simulation, 79*(3), 763–813.

Organ, D., Fleming, M., Terry, T., & Belytschko, T. (1996). Continuous meshless approximations for nonconvex bodies by diffraction and transparency. *Computational Mechanics, 18*(3), 225–235.

Ortiz, M., & Pandolfi, A. (1999). Finite-deformation irreversible cohesive elements for three-dimensional crack-propagation analysis. *International Journal for Numerical Methods in Engineering, 44*(9), 1267–1282.

Rabczuk, T., & Belytschko, T. (2004). Cracking particles: a simplified meshfree method for arbitrary evolving cracks. *International Journal for Numerical Methods in Engineering, 61*(13), 2316–2343.

Rabczuk, T., & Areias, P. (2006). A meshfree thin shell for arbitrary evolving cracks based on an extrinsic basis. *Computer Modeling in Engineering and Sciences, 16*(2), 115–130.

Rabczuk, T., & Zi, G. (2007). A meshfree method based on the local partition of unity for cohesive cracks. *Computational Mechanics, 39*(6), 743–760.

Rabczuk, T., Areias, P., & Belytschko, T. (2007). A meshfree thin shell method for non-linear dynamic fracture. *International Journal for Numerical Methods in Engineering, 72*(5), 524–548.

Rabczuk, T., Bordas, S., & Zi, G. (2007a). A three dimensional large deformation meshfree method for arbitrary evolving cracks". *Computer Methods in Applied Mechanics and Engineering, 196*(29), 2777–2799.

Rabczuk, T., Bordas, S., & Zi, G. (2007b). A three-dimensional meshfree method for continuous multiple crack initiation, nucleation and propagation in statics and dynamics. *Computational Mechanics, 40*(3), 473–495.

Rabczuk, T., Gracie, R., Song, J. H., & Belytschko, T. (2010). Immersed particle method for fluid-structure interaction. *International Journal for Numerical Methods in Engineering, 81*(1), 48–71.

Rabczuk, T., Zi, G., Bordas, S., & Nguyen-Xuan, H. (2008). A geometrically non-linear three-dimensional cohesive crack method for reinforced concrete structures. *Engineering Fracture Mechanics, 75*(16), 4740–4758.

Rabczuk, T., Zi, G., Gerstenberger, A., & Wall, W. A. (2008). A new crack tip element for the phantom-node method with arbitrary cohesive cracks. *International Journal for Numerical Methods in Engineering, 75*(5), 577–599.

Rabczuk, T., Zi, G., Bordas, S., & Nguyen-Xuan, H. (2010). A simple and robust three-dimensional cracking-particle method without enrichment. *Computer Methods in Applied Mechanics and Engineering, 199*(37), 2437–2455.

Remmers, J. J. C., Borst, R. D., & Needleman, A. (2003). A cohesive segments method for the simulation of crack growth. *Computational Mechanics, 31*(1–2), 69–77.

Ren, H., Zhuang, X., Cai, Y., & Rabczuk, T. (2016). Dual-horizon peridynamics. *International Journal for Numerical Methods in Engineering, 108*(12), 1451–1476.

Ren, H., Zhuang, X., Rabczuk, T. (2016). A new peridynamic formulation with shear deformation for elastic solid. *Journal of Micromechanics and Molecular Physics, 01*(02). World Scientific:1650009.

Ren, H., Zhuang, X., & Rabczuk, T. (2017). Dual-horizon peridynamics: A stable solution to varying horizons. *Computer Methods in Applied Mechanics and Engineering, 318*, 762–782.

Rethore, J., Borst, R. D., & Abellan, M. A. (2007). A two-scale approach for fluid flow in fractured porous media. *International Journal for Numerical Methods in Engineering, 71*(7), 780–800.

Silling, S. A., Epton, M., Weckner, O., Xu, J., & Askari, E. (2007). Peridynamic states and constitutive modeling. *Journal of Elasticity, 88*(2), 151–184.

Song, J. H., Areias, P. M. A., & Belytschko, T. (2006). A method for dynamic crack and shear band propagation with phantom nodes. *International Journal for Numerical Methods in Engineering, 67*(6), 868–893.

Vu-Bac, N., Nguyen-Xuan, H., Chen, L., Lee, C. K., Zi, G., Zhuang, X., ... Rabczuk, T. (2013). A method for dynamic crack and shear band propagation with phantom nodes. *International Journal for Numerical Methods in Engineering, 2013*.

Wang, H., & Belytschko, T. (2009). Fluid-structure interaction by the discontinuoussGalerkin method for large deformations. *International Journal for Numerical Methods in Engineering, 77*(1), 30–49.

Zi, G., Rabczuk, T., & Wall, W. (2017). Extended meshfree methods without branch enrichment for cohesive cracks. *Computational Mechanics, 40*(2), 367–382.